




Article

Structural and Magnetic Investigations of the Novel Pyrophosphate $\text{Na}_7\text{Ni}_3\text{Fe}(\text{P}_2\text{O}_7)_4$

Sirine El Arni ¹, Mohammed Hadouchi ^{1,*}, Abderrazzak Assani ¹, Mohamed Saadi ¹, Mimoun El Marssi ², Abdelilah Lahmar ² and Lahcen El Ammari ¹

¹ Laboratoire de Chimie Appliquée des Matériaux, Centre des Sciences des Matériaux, Faculty of Science, Mohammed V University in Rabat, Avenue Ibn Battouta, Rabat BP 1014, Morocco; sirine.elarni@um5r.ac.ma (S.E.A.); a.assani@um5r.ac.ma (A.A.); m.saadi@um5r.ac.ma (M.S.); l.elammari@um5r.ac.ma (L.E.A.)

² Laboratoire de Physique de la Matière Condensée, 33 Rue Saint-Leu, 80033 Amiens, France; mimoun.elmarssi@u-picardie.fr (M.E.M.); abdel.ilah.lahmar@u-picardie.fr (A.L.)

* Correspondence: m.hadouchi@um5r.ac.ma

Abstract: A novel pyrophosphate $\text{Na}_7\text{Ni}_3\text{Fe}(\text{P}_2\text{O}_7)_4$ was synthesized in two distinct forms, single-crystal and powder. Single-crystal X-ray diffraction was used to determine the crystal structure, and powder X-ray diffraction and scanning electron microscopy were used to examine the purity and morphology of the elaborated powder. This phosphate crystallizes in the $\text{P}\bar{1}$ space group of the triclinic system with $a = 6.3677$ (2) Å, $b = 9.3316$ (4) Å, $c = 10.8478$ (4) Å, $\alpha = 65.191$ (1)°, $\beta = 80.533$ (1)° and $\gamma = 73.042$ (1)°. The crystal framework is assembled from the linkage of centrosymmetrical clusters $\text{Ni}_2(\text{Ni}/\text{Fe})_2\text{P}_4\text{O}_{28}$. Each cluster consists of two $(\text{Fe1}/\text{Ni1})\text{O}_6$ octahedra, two Ni_2O_6 octahedra and two P_2O_7 units. The linkage of these clusters is provided by two other P_2O_7 units to generate a three-dimensional structure with distinct tunnels in the [100], [010] and [001] directions, housing the Na^+ cations. The infrared and Raman analyses show the characteristic bands of the pyrophosphate anion $\text{P}_2\text{O}_7^{4-}$. Remarkably, the magnetic investigations revealed the coexistence of two magnetic transitions at ~29 K and ~4.5 K with dominating antiferromagnetic interactions.

Keywords: pyrophosphate; single crystal X-ray diffraction; two magnetic transitions; antiferromagnetic behavior



Citation: El Arni, S.; Hadouchi, M.; Assani, A.; Saadi, M.; El Marssi, M.; Lahmar, A.; El Ammari, L. Structural and Magnetic Investigations of the Novel Pyrophosphate $\text{Na}_7\text{Ni}_3\text{Fe}(\text{P}_2\text{O}_7)_4$. *Magnetochemistry* **2023**, *9*, 162. <https://doi.org/10.3390/magnetochemistry9070162>

Academic Editors: Paula Corte-Leon and Ahmed Talaat

Received: 26 May 2023
Revised: 17 June 2023
Accepted: 20 June 2023
Published: 24 June 2023



Copyright: © 2023 by the authors. Licensee MDPI, Basel, Switzerland. This article is an open access article distributed under the terms and conditions of the Creative Commons Attribution (CC BY) license (<https://creativecommons.org/licenses/by/4.0/>).

1. Introduction

Inorganic materials with layered and tunnel-like structures are currently the subject of intense research across many disciplines, most notably in solid-state chemistry. Among these materials, transition metal phosphates offer a promising field for a variety of applications, including optical, magnetic, and electrochemical ones [1–3]. These materials exhibit an impressively diverse range of structural types associated with various physical and chemical properties. For example, the NASICON (sodium super ionic conductor) material is known for its exceptional ionic conductivity [4], KTP-type compounds (KTiOPO_4) are known for their non-linear optical properties [5] and Olivine structure is favored in lithium batteries due to its high electrochemical activity [6]. However, the basic building unit in these phosphates is the PO_4 tetrahedron. This entity has the flexibility to combine with other PO_4 tetrahedra to generate different units by exchanging oxygen atoms, like P_2O_7 , P_3O_{10} , and $(\text{PO}_3)_\infty$. These various anionic entities give a large and diverse structural family ranging from orthophosphates to polyphosphates [7–9].

Indeed, the focus has been recently directed toward pyrophosphate-based materials because of their rich crystal chemistry and outstanding physical and chemical properties [10–13]. One of the most notable physical properties of pyrophosphates is their high melting points and thermal stability. These characteristics make them ideal candidates for employment in high-temperature applications, such as thermal insulation, solid electrolytes

and refractory materials [14,15]. Additionally, these materials show high potential, high safety and high specific capacity. As a matter of fact, alkali-metal pyrophosphates, specifically lithium and sodium pyrophosphates, have been investigated as cathode materials for sodium-ion batteries (SIBs) and lithium-ion batteries (LIBs), demonstrating good electrochemical activity and high ionic conductivity, making them a suitable electrolyte for (LIBs) and (SIBs). In this context, we can mention the pyrophosphates $\text{Li}_2\text{FeP}_2\text{O}_7$ and $\text{Na}_2\text{FeP}_2\text{O}_7$, which represent remarkable electrochemical performance and excellent thermal stability as cathode materials for LIBs and SIBs [10,16].

Moreover, transition metals pyrophosphates demonstrate intriguing magnetic features. For example, the AFeP_2O_7 , with A, is a monovalent cation (Li, Na, K Rb, Cs and Ag) exhibited an antiferromagnetic phase transition below ambient temperature. These materials demonstrated promising characteristics such as potential ferroelectricity in addition to magnetic ordering and even a possible magnetoelectric effect [17]. Furthermore, the mixed-valence iron pyrophosphate $\text{Fe}_2\text{P}_2\text{O}_7$ showed both ferrimagnetism and spin glass behavior, resulting in disordered magnetic moments of Fe^{2+} and Fe^{3+} ions due to competing exchange behavior [18]. These magnetic properties make these materials appealing for potential applications in various magnetic device technologies. It is worth noting that the magnetic properties vary with the specific transition metals present in the structure as well as the overall crystal structure of these compounds. Whereas the crystal symmetry, the coordination environment and the arrangement of transition metal ions all contribute to determining the resulting magnetic behavior. Additionally, the presence of different transition metals can result in distinct magnetic interactions and spin arrangements [19,20].

As part of studying the structural and magnetic features of new materials, we discuss in the present paper the synthesis of the novel sodium nickel iron pyrophosphate $\text{Na}_7\text{Ni}_3\text{Fe}(\text{P}_2\text{O}_7)_4$ in two distinct forms, single-crystal and powder, as well as its structural characterization and magnetic properties.

2. Materials and Methods

2.1. Synthesis

Single crystals of the novel pyrophosphate $\text{Na}_7\text{Ni}_3\text{Fe}(\text{P}_2\text{O}_7)_4$ were produced by melting a mixture of NaNO_3 ($\geq 99\%$, Merck, Darmstadt, Germany): 0.2735g, $\text{Ni}(\text{NO}_3)_2 \cdot 6\text{H}_2\text{O}$ ($\geq 99\%$, Merck, Darmstadt, Germany): 0.4009g, $\text{Fe}(\text{NO}_3)_3 \cdot 9\text{H}_2\text{O}$ ($\geq 99\%$, AnalaR, Leuven, Belgium): 0.1857g and $\text{NH}_4\text{H}_2\text{PO}_4$ ($\geq 99\%$, AnalaR, Leuven, Belgium): 0.4228g reagents in the molar ratio of Na:Ni:Fe:P = 7:3:1:8. After dissolving the precursors in 75 mL of distilled water, the resultant solution was stirred and held at 353 K until dryness. The collected residue was deposited into a platinum crucible and heated in a furnace to 1163 K, where it remained for two hours before being cooled gradually to 963 K at a rate of 5 K/h. The described procedure yielded yellow single crystals suitable for structure determination. Additional structural details can be acquired through the joint online deposition service provided by CCDC/FIZ Karlsruhe, accessible at <https://www.ccdc.cam.ac.uk/conts/retrieving.html> (accessed on 23 May 2023) by specifying the CSD number 2264902.

The title phosphate was also elaborated as a powder by a sol-gel method, employing the same precursors with identical masses and molar ratios employed to synthesize single crystals. Initial preparation involved dissolving the reagents homogeneously in 75 mL of distilled water with some drops of HNO_3 . Thereafter, citric acid was added to the first solution, in the following molar ratio (Na + Fe + Ni + P): citric acid ($\geq 99\%$, VWR Chemicals, Leuven, Belgium), = 1: 1.5, to chelate the metal ions. The resulting solution was then subjected to evaporation at 353 K to remove the water and generate highly viscous gel. The resultant residue was deposited into an alumina crucible and underwent a series of heat treatments, wherein the temperature was increased in steps of 473 K, 673 K, 873 K, 923 K and, finally, 973 K, with each step lasting for 24 h. A yellow powder was acquired, and its purity was evaluated via X-ray diffraction analysis.

2.2. Characterizations

A suitably sized single crystal was selected under the microscope for the purpose of conducting X-ray diffraction analysis. A Bruker D8 Venture Super DUO diffractometer that is equipped with a PHOTON100 CMOS area-detector and monochromatic MoK α radiation ($\lambda = 0.71073 \text{ \AA}$) was used to collect the diffraction data. Data collection was performed utilizing the APEX3 software [21], and the absorption correction was conducted using the SADABS program through multi-scan semi-empirical process [22]. The crystal structure was initially solved by the direct method with SHELXT 2014 program [23], followed by refinement using the SHELXL 2018 program [24] integrated into the WinGX software [25]. To generate the structural depictions, the DIAMOND software was utilized [26].

Powder X-ray diffraction analysis of the pyrophosphate Na₇Ni₃Fe(P₂O₇)₄ was conducted at ambient temperature utilizing a Shimadzu 6100 diffractometer with Cu K α radiation ($\lambda = 1.5406 \text{ \AA}$). The diffraction data were acquired with a step size of 0.02° and a $2.4^\circ/\text{min}$ scan speed covering an angular range of $10^\circ \leq 2\theta \leq 100^\circ$. The refinement of the experimental powder XRD pattern was performed using Rietveld method with FullProf software package [27]. The morphology and elemental analysis of the powder sample were analyzed using the JEOL JSM-IT100 InTouchScope™ scanning electron microscope (SEM).

The Perkin Elmer RX-I model spectrometer was utilized to register the infrared (FT-IR) spectrum of the Na₇Ni₃Fe(P₂O₇)₄ pyrophosphate within the range of 400 to 4000 cm^{-1} . Additionally, a Renishaw micro-Raman spectrometer was employed to generate the Raman spectrum within the range of 50 – 1300 cm^{-1} . The data were collected using an excitation wavelength of 532 nm to stimulate the powder, while the laser power was carefully set at 0.5 mW to avoid any potential overheating of the sample.

The magnetization versus temperature $M(T)$ and the magnetic field versus magnetization $M(H)$ data of the Na₇Ni₃Fe(P₂O₇)₄ powdered sample (35.2 mg) were collected on a Physical Property Measurements System (PPMS) DynaCool magnetometer. The Temperature-dependent magnetization was recorded using both zero-field-cooled (ZFC) and field-cooled on-cooling (FCC) modes, exploring the temperature range of 2 – 300 K with a step size of 2 K and in various magnetic fields $0.1 \text{ kOe} \leq H \leq 20 \text{ kOe}$. The isothermal magnetization measurements were carried out by applying magnetic fields varying from -90 kOe to 90 kOe at various temperatures ranging from 2 to 300 K . The collected data were corrected from diamagnetism ($-437.6 \times 10^{-6} \text{ emu}\cdot\text{mol}^{-1}$).

3. Results and Discussion

3.1. Crystal Structure

The pyrophosphate Na₇Ni₃Fe(P₂O₇)₄ can be considered a new member of the isostructural family, including Na_{3.64}Ni_{2.18}(P₂O₇)₂, Na_{3.64}Mg_{2.18}(P₂O₇)₂ [28], Na₇Mg_{4.5}(P₂O₇)₄ [29], Na_{2.84}Ag_{1.16}Co₂(P₂O₇)₂ [30], Na_{3.32}Fe_{2.34}(P₂O₇)₂ [31], Ag_{3.68}Co₂(P₂O₇)₂ [32], Na_{3.12}Fe_{2.44}(P₂O₇)₂ [33] and Na₂CoP₂O₇ [34]. Except for the sodium cobalt diphosphate Na₂CoP₂O₇, which crystallizes in the non-centrosymmetric space group P1 because of sodium's deviation from its special position, all the remaining materials exhibit a centrosymmetric structure and crystallize in the $P\bar{1}$ space group. Indeed, the Na₇Ni₃Fe(P₂O₇)₄ pyrophosphate crystallizes in the $P\bar{1}$ space group of the triclinic system with $a = 6.3677 (2) \text{ \AA}$, $b = 9.3316 (4) \text{ \AA}$, $c = 10.8478 (4) \text{ \AA}$, $\alpha = 65.191 (1)^\circ$, $\beta = 80.533 (1)^\circ$, $\gamma = 73.042 (1)^\circ$ and $V = 559.00 (4) \text{ \AA}^3$. A comparison of lattice parameters of some isostructural pyrophosphates is presented in Table 1. In the structure of this pyrophosphate, all atoms occupy the 2i general position of the $P\bar{1}$ space group, excluding for Na2 cation, which is sited in the 1b special Wyckoff position. Importantly, the sites of Na, Ni2, P and O atoms are completely filled, while the Fe1 and Ni1 atoms share equally the 2i Wyckoff position with an occupancy of 50% each. The final structural model results in the following stoichiometric formula Na₇Ni₃Fe(P₂O₇)₄. The obtained low values of the reliability factors attest to the efficacy of this structural model with $R = 2.6\%$, $wR = 6.6\%$ and $S = 1.09$. A summary of the crystal data and parameters obtained from the structure refinement of this phosphate is provided in Table S1 (Supporting Information). The final atomic coordinates and bond valence

sum calculations (BVS) can be found in Table S2, the anisotropic atomic displacement parameters and the selected bond distances and angles are displayed in Tables S3 and S4, respectively. The bond valence sums are in line with the expected oxidation state of each atom in the structure.

Table 1. Lattice parameters comparison of some reported $\text{Na}_7\text{Ni}_3\text{Fe}(\text{P}_2\text{O}_7)_4$ isotypes.

Compounds	Lattice Parameters						Space Group	Ref.
	a (Å)	b (Å)	c (Å)	α (°)	β (°)	γ (°)		
$\text{Na}_7\text{Mg}_{4.5}(\text{P}_2\text{O}_7)_4$	6.3932 (7)	9.4219 (10)	10.9116 (10)	64.711 (7)	80.374 (8)	73.543 (7)	$\text{P}\bar{1}$	[29]
$\text{Na}_{3.32}\text{Fe}_{2.34}(\text{P}_2\text{O}_7)_2$	6.4106 (6)	9.3948 (0)	10.9795 (6)	64.965 (1)	86.005 (0)	73.054 (8)	$\text{P}\bar{1}$	[31]
$\text{Ag}_{3.68}\text{Co}_2(\text{P}_2\text{O}_7)_2$	6.521 (4)	9.623 (6)	10.969 (7)	64.23 (2)	80.14 (3)	72.10 (2)	$\text{P}\bar{1}$	[32]
$\text{Na}_{3.12}\text{Fe}_{2.44}(\text{P}_2\text{O}_7)_2$	6.424 (2)	9.440 (1)	10.981 (2)	64.77 (1)	86.21 (2)	73.13 (2)	$\text{P}\bar{1}$	[33]
$\text{Na}_7\text{Ni}_3\text{Fe}(\text{P}_2\text{O}_7)_4$	6.3677 (2)	9.3316 (4)	10.8478 (4)	65.191 (1)	80.533 (1)	73.042 (1)	$\text{P}\bar{1}$	This work

In the structure of this phosphate, the two P_2O_7 groups each adopt an almost eclipsed configuration and the angles $\text{P}(1)\text{-O}(3)\text{-P}(3)^{\text{ix}}$ and $\text{P}(2)\text{-O}(8)\text{-P}(4)^{\text{vi}}$ of $132.97(8)^\circ$, $124.54(7)^\circ$, respectively. However, we note that the $\text{P}(1)\text{O}_4$ and $\text{P}(2)\text{O}_4$ tetrahedra are more regular than the $\text{P}(3)\text{O}_4$ and $\text{P}(4)\text{O}_4$ tetrahedra (see Table S4). Moreover, the structure of this phosphate consists of two octahedra (Fe1/Ni1O_6 and Ni2O_6) sharing a corner and forming the $\text{Ni}(\text{Fe/Ni})\text{O}_{11}$ group. The latter is connected on one side to the P_2O_7 group by sharing an edge, while on the other side, the $\text{Ni}(\text{Fe/Ni})\text{O}_{11}$ group is linked to another diphosphate P_2O_7 by sharing corners. The junction between two $\text{Ni}(\text{Fe/Ni})\text{O}_{11}$ groups is provided by two diphosphate units $\text{P}(1)\text{P}(3)\text{O}_7$ and $\text{P}(3)\text{P}(1)\text{O}_7$, leading to the formation of $\text{Ni}_2(\text{Fe/Ni})_2\text{P}_4\text{O}_{28}$ cluster (see Figure 1). The interconnection between these clusters is ensured by two other diphosphate groups, $\text{P}(2)\text{P}(4)\text{O}_7$ and $\text{P}(4)\text{P}(2)\text{O}_7$, sharing corners with $(\text{Fe1/Ni1})\text{O}_6$ and Ni2O_6 octahedra generating three-dimensional framework as shown in Figure 1. The latter reveals the existence of distinct tunnels in [100], [010] and [001] directions, housing the Na^+ cations as depicted in Figure 2. A similar arrangement is found in the structure of the diphosphates $(\text{Na}_{0.71}\text{Ag}_{0.29})_2\text{CoP}_2\text{O}_7$ [30], $\text{Ag}_{3.68}\text{Co}_2(\text{P}_2\text{O}_7)_2$ [32], and $\text{Na}_{3.12}\text{Fe}_{2.44}(\text{P}_2\text{O}_7)_2$ [33]. In the latter compound, the tunnels are filled with Na and Fe atoms, with some of them occupying partially or mixed sites, while for the $\text{Na}_7\text{Ni}_3\text{Fe}(\text{P}_2\text{O}_7)_4$, the tunnels accommodate only Na cations. It is worth noting that Na1 and Na2 atoms show relatively elongated thermal ellipsoids, and this is likely due to the distortion present in the Na sites. Notably, the distortion calculations reveal that Na1 and Na2 sites exhibit a high degree of distortion compared to Na3 and Na4 sites (refer to Table S4).

3.2. Powder X-ray Diffraction and Scanning Electron Microscopy

To assess the purity of the polycrystalline form of the $\text{Na}_7\text{Ni}_3\text{Fe}(\text{P}_2\text{O}_7)_4$ pyrophosphate, a refinement of the XRD pattern was performed utilizing the Rietveld technique [35]. The structural parameters obtained from the single crystal study were utilized as the initial model for the refinement process. After optimizing the profile parameters, the structural parameters were refined. The pseudo-Voigt function was employed to accurately assimilate the shape of XRD peaks. Figure 3a demonstrates a notable fit between the experimental and the calculated patterns, as evidenced by the satisfactory R-values, thereby confirming the produced powder pure phase. The refined unit cell parameters are presented in Table S5. A summary of the Rietveld refined crystallographic parameters, including the atomic positions and isotropic displacement parameters, can be found in Table S6. The selected bond distances and angles obtained from the Rietveld refinement are displayed in Table S7.

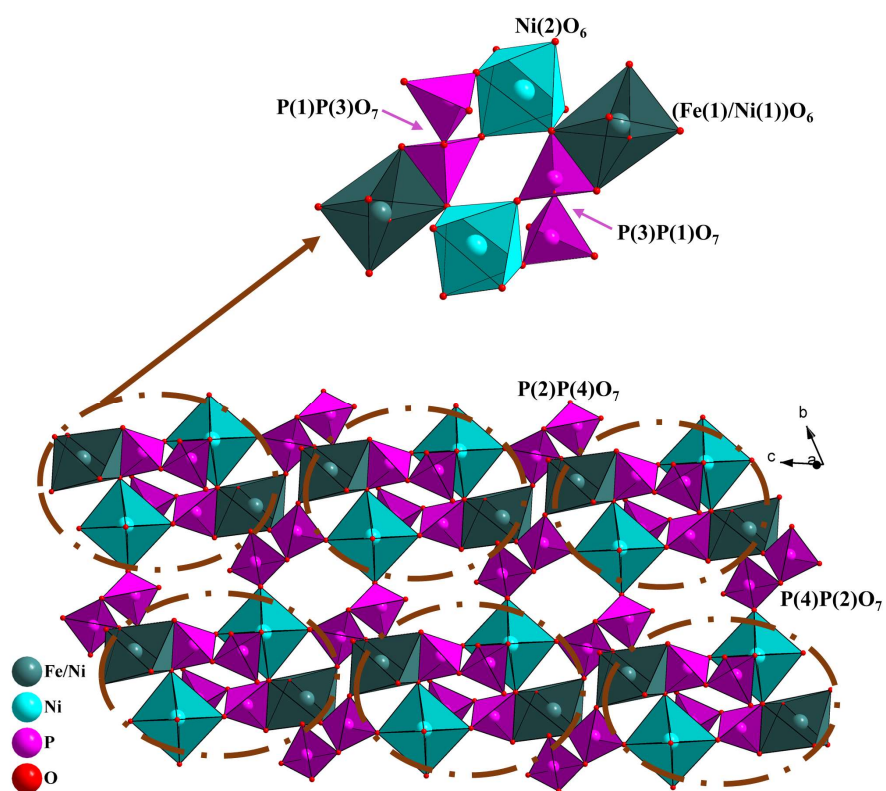


Figure 1. Junction between clusters provided by diphosphate groups in the bc plane of the $\text{Na}_7\text{Ni}_3\text{Fe}(\text{P}_2\text{O}_7)_4$ pyrophosphate.

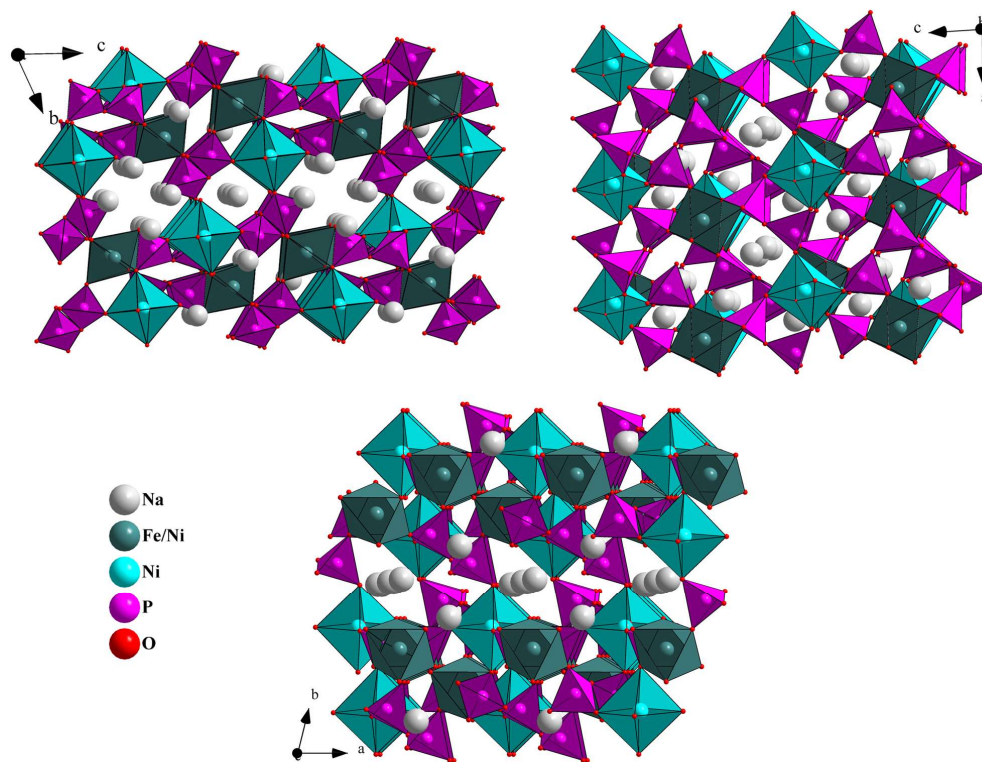


Figure 2. Projection along the a , b and c directions reveals the presence of distinct tunnels in $\text{Na}_7\text{Ni}_3\text{Fe}(\text{P}_2\text{O}_7)_4$ structure.

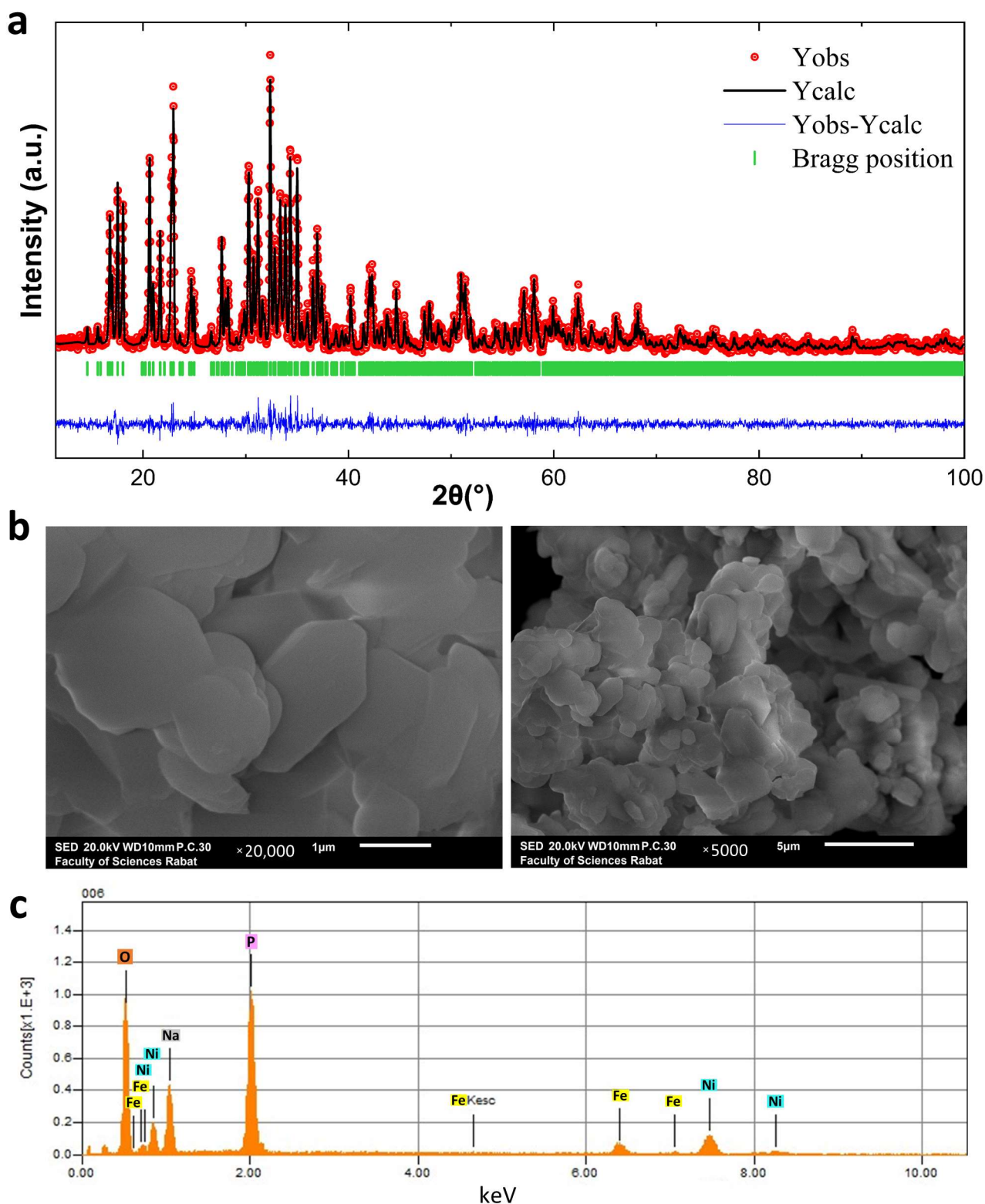


Figure 3. (a) XRD powder pattern refined with Rietveld method. (b) Scanning electron microscopy images of the as-synthesized $\text{Na}_7\text{Ni}_3\text{Fe}(\text{P}_2\text{O}_7)_4$ powder. (c) EDS spectrum displaying the elemental composition of $\text{Na}_7\text{Ni}_3\text{Fe}(\text{P}_2\text{O}_7)_4$.

The scanning electron microscopy (SEM) micrographs of the polycrystalline sample reveal the presence of irregularly formed particles with micrometer-scale sizes (Figure 3b). The energy-dispersive X-ray spectroscopy (EDS) analysis confirms that the powder exhibits

a homogeneous dispersal with the presence of Na, Ni, Fe, P and O atoms only. Moreover, the atomic ratio of these elements closely aligned with the desired composition, as evidenced by the Na/Fe, Ni/Fe and P/Fe ratios of 7.01, 3.09 and 7.99, respectively (Figure 3c).

The average crystallite size can be estimated from XRD data using the Debye–Scherrer equation: $D_{SC} = K\lambda/\beta \cos \theta$ [36]. D_{SC} represents the average crystallite size (nm), K denotes the Scherrer constant approximately equal to 0.9, λ corresponds to the wavelength of the X-ray radiation, β is the FWHM of the intense diffraction peaks (radians) and θ is the peak diffraction angle. Using the three most intense peaks (122), (130) and (030)), the obtained average crystallite size is 40.24 nm.

3.3. FT-Infrared and Raman Spectroscopy

The FT-IR and Raman vibrational spectra of the studied phosphate are illustrated in Figure 4. The vibration of the $[P_2O_7]^{4-}$ moieties can be viewed as a combination of P–O, P–O–P, and O–P–O vibrations. For the infrared spectrum, the bands observed at high frequencies, specifically 1154 cm^{-1} and 1094 cm^{-1} , can be ascribed to the P–O asymmetric stretching vibrations (ν_{as}), whereas the band located at 1034 cm^{-1} can be attributed to the P–O symmetric stretching vibrations (ν_s) within the PO_3 groups of the diphosphate units. Additionally, the bands located between 999 and 897 cm^{-1} are related to the asymmetric stretching vibration (ν_{as}) of P–O–P, while the one seen at 737 cm^{-1} is attributed to the symmetric stretching vibration (ν_s) of P–O–P bridges. Moreover, the absorption peaks in the range of 600 – 699 cm^{-1} correspond to the asymmetric bending vibration (δ_{as}) of O–P–O, whereas the low bands at less than 600 cm^{-1} could be ascribed to O–P–O symmetric bending mode (δ_s). All the suggested assignments for the vibrational modes of P_2O_7 groups are consistent with those of pyrophosphates reported previously [37–39].

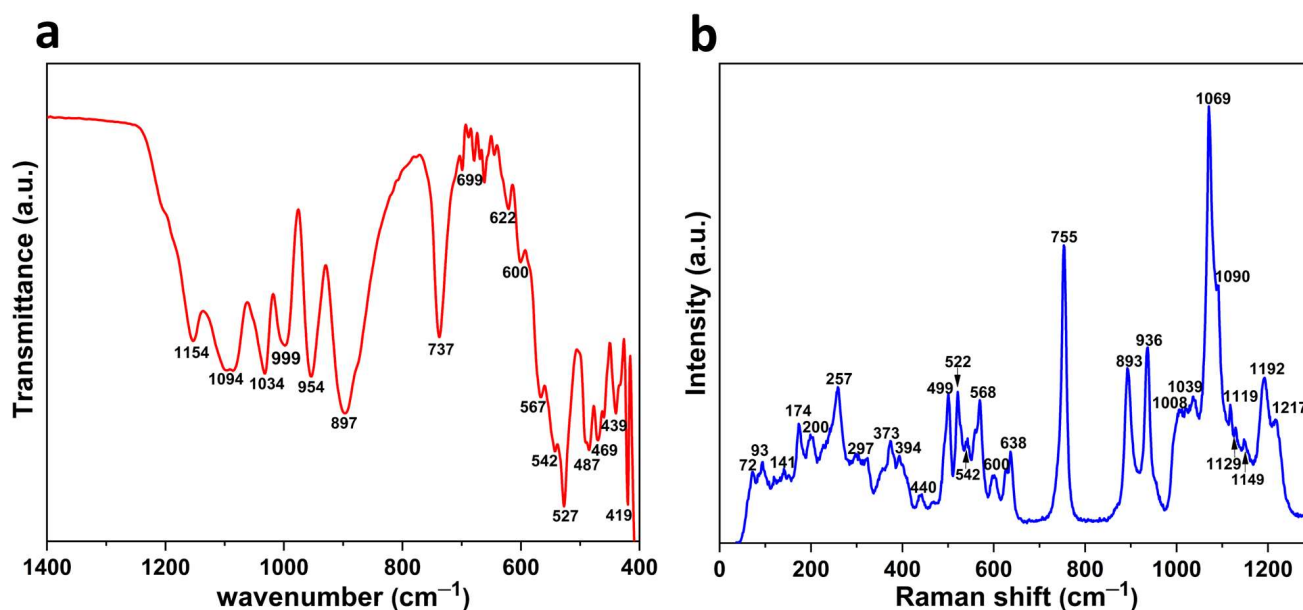


Figure 4. FT-IR (a) and Raman (b) vibrational spectra of $Na_7Ni_3Fe(P_2O_7)_4$ powder.

The assignment of the Raman data in the region 400 – 1300 cm^{-1} resembles closely to that of the IR spectrum. As a result, the strong Raman bands noticed within 1217 and 1090 cm^{-1} can be attributed to P–O asymmetric stretching vibrations (ν_{as}), whereas the bands observed between 1090 and 1008 cm^{-1} can be attributed to P–O symmetric stretching vibrations (ν_s) within the PO_3 groups of diphosphate units. Furthermore, the bands located between 1008 and 893 cm^{-1} can be attributed to the asymmetric stretching vibration (ν_{as}) of P–O–P bridges, while that seen at 755 cm^{-1} is assigned to the symmetric stretching vibration (ν_s) of P–O–P bridges. The Raman bands located in the region between 373 – 600 cm^{-1} can be ascribed to O–P–O bending modes: the bands observed at 638 and

600 cm^{-1} are attributed to the asymmetric bending vibration (δ_{as}) of O–P–O, whereas the bands located at 568–373 cm^{-1} region originate from the O–P–O symmetric bending mode (δ_{s}). The low-frequency bands below 300 cm^{-1} can be identified as lattice vibrations which mainly arise from the external modes [40]. These distinctive peaks provide more evidence of the presence of P_2O_7 dimers in this phosphate.

3.4. Magnetic Behavior

The resulting magnetic susceptibility ($\chi = M/H$) in a magnetic field of 0.1 kOe is illustrated in Figure 5a. The inverse magnetic susceptibility $\chi^{-1}(T)$ is presented in Figure 5b.

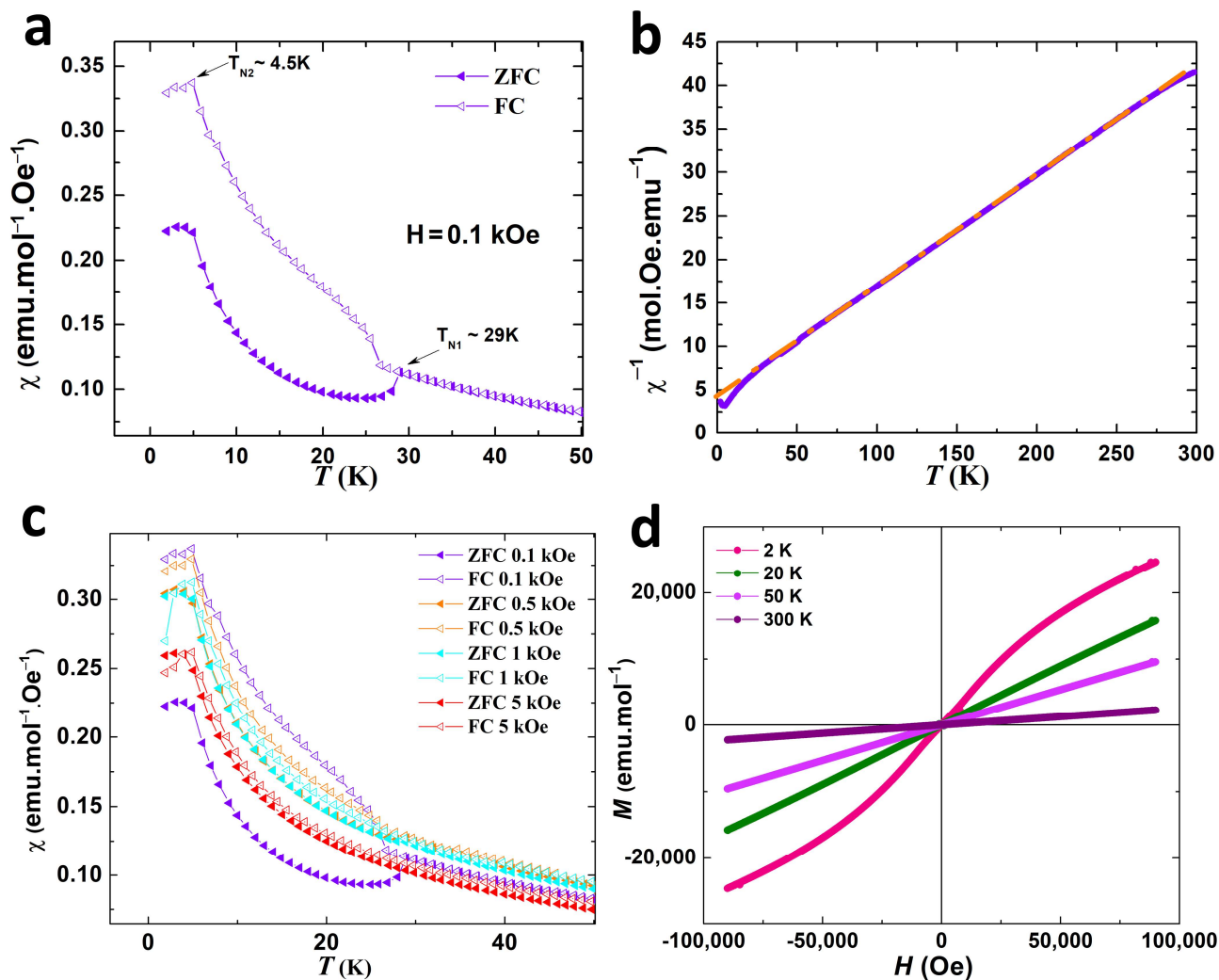


Figure 5. (a) χ vs. T of $\text{Na}_7\text{Ni}_3\text{Fe}(\text{P}_2\text{O}_7)_4$ in ZFC and FC modes at $H = 0.1\text{kOe}$. (b) χ^{-1} vs. T data; the orange dotted line is the fit of the Curie–Weiss law (refer to the text). (c) The magnetic susceptibility as a function of temperature in in ZFC and FCC regimes in various magnetic fields up to 5 kOe. (d) M vs. H curves of $\text{Na}_7\text{Ni}_3\text{Fe}(\text{P}_2\text{O}_7)_4$ at various temperatures.

As depicted in Figure 5a, the magnetic susceptibility (χ) in the $\text{Na}_7\text{Ni}_3\text{Fe}(\text{P}_2\text{O}_7)_4$ compound reveals two distinctive features. Firstly, a broad peak is observed at approximately 29 K, indicating the occurrence of antiferromagnetic ordering. As the temperature further decreases, a second notable sharp increase in susceptibility is observed around 4.5 K, followed by a sudden decline at approximately 3.5 K. This behavior is indicative of the presence of antiferromagnetic ordering of another sublattice. The magnetic anomaly observed at ~ 29 K decreases and disappears at higher applied magnetic fields (≥ 1 kOe) (Figure 5c). This confirms that the first sublattice ordering is more susceptible to applied

magnetic fields, resulting in significant variations in susceptibility as a function of the magnetic field.

In the high-temperature zone, $\chi^{-1}(T)$ obeys the Curie–Weiss law: $\chi(T) = C/(T - \theta_{cw})$, where C and θ_{cw} represent the Curie constant and Weiss temperature, respectively (Figure 5b). Therefore, the resulting Weiss temperature is $\theta_{cw} = -33.8$ K, and the obtained Curie constant is $C = 7.87$ emu K mol⁻¹ per formula unit, which gives an effective magnetic moment of $\mu_{eff} = 7.93$ μ_B . This obtained effective experimental moment is in accordance with the theoretically calculated one $\mu_{eff} = \sqrt{3(\mu_{eff}(\text{Ni}^{2+}))^2 + (\mu_{eff}(\text{Fe}^{3+}))^2} = 7.68$ μ_B based on Ni²⁺ ($t_{2g}^6 e_g^2$, $S = 1$, $\mu_{eff}(\text{Ni}^{2+}) = 2.828$ μ_B) and Fe³⁺ ($t_{2g}^3 e_g^2$, $S = 5/2$, $\mu_{eff}(\text{Fe}^{3+}) = 5.916$ μ_B). The negative Weiss temperature suggests that antiferromagnetic interactions are predominating in the material. The $\chi(T)$ curves show a noticeable bifurcation between the ZFC and FC regimes, indicating the possibility of a spin-glass state at lower temperatures, as previously reported on nickel-iron phosphate K₄NiFe₃(PO₄)₅ [41]. This divergence decreases with increasing magnetic field and approaches convergence at 5 kOe (Figure 5c). This magnetic behavior can be attributed to the occurrence of spin frustration, which decreases when a high magnetic field is applied since a higher field strength can direct more magnetic spins even at lower temperatures. This is evident from the frustration ratio, $f = (|\theta_{cw}/T_N|) = 1.16$ [42,43].

To elucidate the magnetic state of this pyrophosphate, isothermal magnetization as a function of the magnetic field (M vs. H) was measured at various temperatures from 2 K to 300 K in the field range of -90 kOe and 90 kOe. A selection of $M(H)$ curves is presented in Figure 5d, revealing an S-shaped $M(H)$ curve at 2K indicating the AFM order.

Considering the structural features displayed by this pyrophosphate, various exchange pathways could potentially contribute to the observed magnetic behavior. The most dominant interactions occur within Ni₂(Fe/Ni)₂P₄O₂₈ clusters, which are built up from (Fe1/Ni1)O₆ and Ni₂O₆ octahedra sharing a corner and forming the Ni(Fe/Ni)O₁₁ group. This group is connected on one side to the P₂O₇ dimer by sharing an edge and on the other side to another diphosphate P₂O₇ by sharing corners, as illustrated in Figure 1. Within the clusters, there are various magnetic superexchange interactions, one of which implies the corner sharing between (Fe1/Ni1)O₆ and Ni₂O₆ octahedra, the distance between the centers is 3.67 Å and the angle (Ni1/Fe1)–O–Ni is 118.7°. This lead to the Fe(1)–O–Ni(2) and Ni(1)–O–Ni(2) AFM superexchange interactions [44]. Another pathway involves the magnetic couplings via the PO₄ groups resulting in competition between Ni–O–P–O–Ni and Ni–O–P–O–Fe superexchange interactions, which are all required to be antiferromagnetic according to GKA rules [45,46]. The third exchange pathway involves the coupling between consecutive clusters via PO₄ groups, which should be antiferromagnetic consistently, with the overall antiferromagnetic behavior comparable to that reported for other transition metal phosphates [47,48].

4. Conclusions

In summary, the Na₇Ni₃Fe(P₂O₇)₄ pyrophosphate was synthesized in two distinct forms, single-crystal and powder. This synthesized powder was analyzed through X-ray diffraction, SEM, FTIR and Raman spectroscopies. It crystallizes in the P $\bar{1}$ the space group of the triclinic system and its structure has an open framework with distinct tunnels in the [100], [010] and [001] directions, housing the Na⁺ cations. The magnetic measurements uncovered the presence of a distinct AFM ordering at 4.5 K, which is preceded by another sublattice AFM ordering around 29 K.

Supplementary Materials: The following supporting information can be downloaded at: <https://www.mdpi.com/article/10.3390/magnetochemistry9070162/s1>. Table S1: Crystal data, data collection and structure refinement for $\text{Na}_7\text{Ni}_3\text{Fe}(\text{P}_2\text{O}_7)_4$. Table S2: Atomic coordinates and equivalent isotropic displacement parameters (\AA^2) for $\text{Na}_7\text{Ni}_3\text{Fe}(\text{P}_2\text{O}_7)_4$ obtained by Single-Crystal X-ray Diffraction. Table S3: Anisotropic atomic displacement parameters (\AA^2) for $\text{Na}_7\text{Ni}_3\text{Fe}(\text{P}_2\text{O}_7)_4$. Table S4: Selected interatomic distances (\AA) and angles ($^\circ$) for $\text{Na}_7\text{Ni}_3\text{Fe}(\text{P}_2\text{O}_7)_4$. Table S5: Rietveld refined parameters of $\text{Na}_7\text{Ni}_3\text{Fe}(\text{P}_2\text{O}_7)_4$ powder. Table S6: Atomic positions, isotropic displacement parameters for $\text{Na}_7\text{Ni}_3\text{Fe}(\text{P}_2\text{O}_7)_4$ obtained by Rietveld refinement. Table S7: Selected interatomic distances (\AA) and angles ($^\circ$) for $\text{Na}_7\text{Ni}_3\text{Fe}(\text{P}_2\text{O}_7)_4$ obtained by Rietveld refinement.

Author Contributions: Conceptualization, S.E.A. and M.H.; methodology, M.H.; software, S.E.A., M.H., A.L. and L.E.A.; validation, A.A., M.S., A.L., M.E.M. and L.E.A.; formal analysis, S.E.A. and M.H.; investigation, S.E.A. and M.H.; resources, M.S. and M.E.M.; data curation, S.E.A., A.L. and L.E.A.; writing—original draft preparation, S.E.A.; writing—review and editing, M.H., A.L. and L.E.A.; visualization, S.E.A., M.H. and L.E.A.; supervision, M.H. and A.A.; project administration, M.H. and A.A.; funding acquisition, A.A., M.S. and M.E.M. All authors have read and agreed to the published version of the manuscript.

Funding: This research was funded by the Excellence Research Scholarships Program of the CNRST of the Kingdom of Morocco, grant number 23UM5R2021.

Institutional Review Board Statement: Not applicable.

Informed Consent Statement: Not applicable.

Data Availability Statement: The Crystallographic Data have been submitted as a cif file in the Data Center with the CSD number 2264902. A free download of the data is available through <http://www.ccdc.cam.ac.uk/conts/retrieving.html> (accessed on 23 May 2023), or from the Cambridge Crystallographic Data Centre, 12 Union Road, Cambridge CB2 1EZ, UK; Fax: +44-1223-336-033; or by e-mail: deposit@ccdc.cam.ac.uk.

Acknowledgments: The X-ray measurements were kindly provided by the Faculty of Science, Mohammed V University, which the authors sincerely thank.

Conflicts of Interest: The authors declare no conflict of interest.

References

1. Gopalakrishnan, J.; Rangan, K.K.; Prasad, B.R.; Subramanian, C.K. New Transition Metal Phosphates Related to KTiOPO_4 . Synthesis of $\text{K}_{0.5}\text{M}_{0.5}\text{M}'_{0.5}\text{OPO}_4$ ($\text{M} = \text{Nb}, \text{Ta}$; $\text{M}' = \text{Ti}, \text{V}$) and $\text{K}_{1-x}\text{Ti}_{1-x}\text{V}_x\text{OPO}_4$ Exhibiting Nonlinear Optical Behavior. *J. Solid State Chem.* **1994**, *111*, 41–47. [[CrossRef](#)]
2. Dai, D.; Whangbo, M.-H.; Koo, H.-J.; Rocquefelte, X.; Jolic, S.; Villesuzanne, A. Analysis of the Spin Exchange Interactions and the Ordered Magnetic Structures of Lithium Transition Metal Phosphates LiMPO_4 ($\text{M} = \text{Mn}, \text{Fe}, \text{Co}, \text{Ni}$) with the Olivine Structure. *Inorg. Chem.* **2005**, *44*, 2407–2413. [[CrossRef](#)] [[PubMed](#)]
3. García-Moreno, O.; Alvarez-Vega, M.; García-Alvarado, F.; García-Jaca, J.; Gallardo-Amores, J.M.; Sanjuán, M.L.; Amador, U. Influence of the Structure on the Electrochemical Performance of Lithium Transition Metal Phosphates as Cathodic Materials in Rechargeable Lithium Batteries: A New High-Pressure Form of LiMPO_4 ($\text{M} = \text{Fe}$ and Ni). *Chem. Mater.* **2001**, *13*, 1570–1576. [[CrossRef](#)]
4. Chen, S.; Wu, C.; Shen, L.; Zhu, C.; Huang, Y.; Xi, K.; Maier, J.; Yu, Y. Challenges and Perspectives for NASICON-Type Electrode Materials for Advanced Sodium-Ion Batteries. *Adv. Mater.* **2017**, *29*, 1700431. [[CrossRef](#)] [[PubMed](#)]
5. Yang, F.; Wang, L.; Huang, L.; Zou, G. The study of structure evolution of KTiOPO_4 family and their nonlinear optical properties. *Coord. Chem. Rev.* **2020**, *423*, 213491. [[CrossRef](#)]
6. Gong, C.; Xue, Z.; Wen, S.; Ye, Y.; Xie, X. Advanced carbon materials/olivine LiFePO_4 composites cathode for lithium ion batteries. *J. Power Sources* **2016**, *318*, 93–112. [[CrossRef](#)]
7. Wang, Y.; Pan, S.; Yu, H.; Su, X.; Zhang, M.; Zhang, F.; Han, J. $\text{Cs}_4\text{Mo}_5\text{P}_2\text{O}_{22}$: A first Strandberg-type POM with 1D straight chains of polymerized $[\text{Mo}_5\text{P}_2\text{O}_{23}]^{6-}$ Units and moderate second harmonic generation response. *Chem. Commun.* **2013**, *49*, 306–308. [[CrossRef](#)]
8. Gezović, A.; Vujković, M.J.; Milović, M.; Grudić, V.; Dominko, R.; Mentus, S. Recent developments of $\text{Na}_4\text{M}_3(\text{PO}_4)_2(\text{P}_2\text{O}_7)$ as the cathode material for alkaline-ion rechargeable batteries: Challenges and outlook. *Energy Storage Mater.* **2021**, *37*, 243–273. [[CrossRef](#)]
9. Arbi, K.; Hassen-Chehimi, D.B.; Trabelsi-Ayadi, M.; Silvestre, J. Structure refinement of potassium–samarium cyclotetraphosphate $\text{KSmP}_4\text{O}_{12}$. *Mater. Res. Bull.* **2000**, *35*, 1533–1539. [[CrossRef](#)]
10. Barpanda, P.; Nishimura, S.I.; Yamada, A. High-Voltage Pyrophosphate Cathodes. *Adv. Energy Mater.* **2012**, *2*, 841–859. [[CrossRef](#)]

11. Polnišer, R.; Štolcová, M.; Hronec, M.; Mikula, M. Structure and reactivity of copper iron pyrophosphate catalysts for selective oxidation of methane to formaldehyde and methanol. *Appl. Catal. A Gen.* **2011**, *400*, 122–130. [CrossRef]
12. Villain, S. Ionic conductivity of pure sodium pyrophosphate $\text{Na}_4\text{P}_2\text{O}_7$. *Solid State Ion.* **1999**, *116*, 73–83. [CrossRef]
13. Béjaoui, A.; Horchani-Naifer, K.; Hajji, M.; Férid, M. Crystal structure, physical properties and bond valence analysis of NaLuP_2O_7 . *Solid State Sci.* **2014**, *31*, 46–53. [CrossRef]
14. Li, S.; Li, Y.; Xu, N.; Li, S.; Zhong, N.; Fu, C.; Luo, H.; Wang, H. Novel ZrP_2O_7 ceramic foams with controllable structures and ultra-low thermal conductivity. *J. Eur. Ceram. Soc.* **2021**, *41*, 7233–7240. [CrossRef]
15. Zhao, Z.; Xiang, H.; Dai, F.-Z.; Peng, Z.; Zhou, Y. $(\text{TiZrHf})\text{P}_2\text{O}_7$: An equimolar multicomponent or high entropy ceramic with good thermal stability and low thermal conductivity. *J. Mater. Sci. Technol.* **2019**, *35*, 2227–2231. [CrossRef]
16. Niu, Y.; Zhang, Y.; Xu, M. A review on pyrophosphate framework cathode materials for sodium-ion batteries. *J. Mater. Chem. A* **2019**, *7*, 15006–15025. [CrossRef]
17. Gentil, S.; Andreica, D.; Lujan, M.; Rivera, J.-P.; Kubel, F.; Schmid, H. Synthesis, structure and magnetic susceptibility of KCrP_2O_7 , a potential antiferromagnetic magnetoelectric. *Ferroelectrics* **1997**, *204*, 35–44. [CrossRef]
18. Adam, L.; Pautrat, A.; Perez, O.; Boullay, P. Contrasted role of disorder for magnetic properties in an original mixed-valency iron phosphate. *Phys. Rev. B* **2010**, *82*, 054401. [CrossRef]
19. Natarajan, S.; Mandal, S. Open-framework structures of transition-metal compounds. *Angew. Chem.-Int. Ed.* **2008**, *47*, 4798–4828. [CrossRef]
20. Shvanskaya, L.V.; Volkova, O.S.; Vasiliev, A.N. A review on crystal structure and properties of 3d transition metal (II) orthophosphates $\text{M}_3(\text{PO}_4)_2$. *J. Alloys Compd.* **2020**, *835*, 155028. [CrossRef]
21. Bruker-Nonius, SAINT-Plus, version 7.06a; Bruker AXS Inc.: Madison, WI, USA, 2004.
22. Sheldrick, G.M. SADABS Version 2004/1; A Program for Empirical Absorption Correction; University of Göttingen: Göttingen, Germany, 2004.
23. Sheldrick, G.M. SHELXT—Integrated space-group and crystal-structure determination. *Acta Crystallogr. Sect. A Found. Adv.* **2015**, *71*, 3–8. [CrossRef]
24. Sheldrick, G.M. Crystal structure refinement with SHELXL. *Acta Crystallogr. Sect. C Struct. Chem.* **2015**, *71*, 3–8. [CrossRef]
25. Farrugia, L.J. WinGX and ORTEP for Windows: An update. *J. Appl. Crystallogr.* **2012**, *45*, 849–854. [CrossRef]
26. Putz, H. Diamond-crystal and molecular structure visualization crystal impact. *Rathausgasse* **2014**, *30*, 1997–2000.
27. Rodríguez-Carvajal, J. Magnetic structure determination from powder diffraction using the program Fullprof. In *Applied Crystallography*; World Scientific: Singapore, 2001; pp. 30–36. [CrossRef]
28. Erragh, F.; Boukhari, A.; Abraham, F.; Elouadi, B. Study of the Crystal Structures of Sodium Magnesium and Sodium Nickel Diphosphates. *J. Solid State Chem.* **2000**, *152*, 323–331. [CrossRef]
29. Ma, R.; Yang, Y.; Pan, S.; Sun, Y.; Yang, Z. Structure comparison and optical properties of $\text{Na}_7\text{Mg}_{4.5}(\text{P}_2\text{O}_7)_4$: A sodium magnesium phosphate with isolated P_2O_7 units. *New J. Chem.* **2017**, *41*, 3399–3404. [CrossRef]
30. Marzouki, R.; Guesmi, A.; Zid, M.F.; Driss, A. Synthesis, Crystal Structure and Electrical Properties of a New Mixed Compound $(\text{Na}_{0.71}\text{Ag}_{0.29})_2\text{CoP}_2\text{O}_7$. *Cryst. Struct. Theory Appl.* **2012**, *01*, 68–73. [CrossRef]
31. Chen, M.; Chen, L.; Hu, Z.; Liu, Q.; Zhang, B.; Hu, Y.; Gu, Q.; Wang, J.; Wang, L.; Guo, X.; et al. Carbon-Coated $\text{Na}_{3.32}\text{Fe}_{2.34}(\text{P}_2\text{O}_7)_2$ Cathode Material for High-Rate and Long-Life Sodium-Ion Batteries. *Adv. Mater.* **2017**, *29*, 1605535. [CrossRef]
32. Moussa, M.A.B. Synthesis and Structure of New Mixed Silver Cobalt(II)/(III) Diphosphate- $\text{Ag}_{3.68}\text{Co}_2(\text{P}_2\text{O}_7)_2$. Silver(I) Transport in the Crystal. *Int. J. Electrochem. Sci.* **2019**, *14*, 1500–1515. [CrossRef]
33. Angenault, J.; Couturier, J.-C.; Quarton, M.; Robert, F. Structure of $\text{Na}_{3.12}\text{Fe}_{2.44}(\text{P}_2\text{O}_7)_2$. *Eur. J. Solid State Inorg. Chem.* **1995**, *32*, 335–343.
34. Materials Data on $\text{Na}_2\text{CoP}_2\text{O}_7$ by Materials Project. 2016. Available online: <https://www.osti.gov/dataexplorer/servlets/purl/1328091> (accessed on 15 June 2023).
35. Rietveld, H.M. A profile refinement method for nuclear and magnetic structures. *J. Appl. Crystallogr.* **1969**, *2*, 65–71. [CrossRef]
36. Klug, H.P.; Alexander, L.E. *X-ray Diffraction Procedures: For Polycrystalline and Amorphous Materials*, 2nd ed.; Wiley: Hoboken, NJ, USA, 1974.
37. Lamsaf, H.; Fausto, R.; Costa, B.F.O.; Toyir, J.; Elghadraoui, E.H.; Ijjaali, M.; Oulmekki, A. Synthesis and physicochemical characterization of a new mixed-valence Iron(III)-Zinc(II) diphosphate: $\text{Zn}^{2+}\text{Fe}^{3+}_2(\text{P}_2\text{O}_7)_2$. *Mater. Chem. Phys.* **2018**, *216*, 22–27. [CrossRef]
38. Bosacka, M.; Blonska-Tabero, A.; Filipek, E.; Luxová, J.; Šulcová, P. Synthesis and characterization of $\text{Co}_5\text{Cr}_2(\text{P}_2\text{O}_7)_4$ —New pyrophosphate as a colouring substance. *Ceram. Int.* **2021**, *47*, 24607–24614. [CrossRef]
39. Song, Z.; Yu, H.; Wu, H.; Hu, Z.; Wang, J.; Wu, Y. Syntheses, structures and characterization of non-centrosymmetric $\text{Rb}_2\text{Zn}_3(\text{P}_2\text{O}_7)_2$ and centrosymmetric $\text{Cs}_2\text{M}_3(\text{P}_2\text{O}_7)_2$ ($\text{M} = \text{Zn}$ and Mg). *Inorg. Chem. Front.* **2020**, *7*, 3482–3490. [CrossRef]
40. Scholz, R.; Frost, R.L.; Xi, Y.; Graça, L.M.; Lagoeiro, L.; López, A. Vibrational spectroscopic characterization of the phosphate mineral phosphophyllite— $\text{Zn}_2\text{Fe}(\text{PO}_4)_2 \cdot 4\text{H}_2\text{O}$, from Hagendorf Süd, Germany and in comparison with other zinc phosphates. *J. Mol. Struct.* **2013**, *1039*, 22–27. [CrossRef]
41. El Arni, S.; Hadouchi, M.; Assani, A.; Saadi, M.; Lahmar, A.; El Marssi, M.; Koketsu, T.; El Ammari, L. A novel phosphate, $\text{K}_4\text{NiFe}_3(\text{PO}_4)_5$: Synthesis, crystal structure and magnetic properties. *J. Solid State Chem.* **2022**, *313*, 123333. [CrossRef]

42. Hadouchi, M.; Assani, A.; Saadi, M.; Kopelevich, Y.; da Silva, R.R.; Lahmar, A.; Bouyanfif, H.; El Marssi, M.; El Ammari, L. Unconventional spin-glass-like state in $\text{AgCo}_2\text{V}_3\text{O}_{10}$, the novel magnetically frustrated material. *J. Magn. Magn. Mater.* **2019**, *491*, 165623. [[CrossRef](#)]
43. Hadouchi, M.; Assani, A.; Saadi, M.; Lahmar, A.; El Marssi, M.; El Ammari, L. Magnetic properties of a new cobalt hydrogen vanadate with a dumortierite-like structure: $\text{Co}_{13.5}(\text{OH})_6(\text{H}_{0.5}\text{VO}_{3.5})_2(\text{VO}_4)_6$. *Acta Crystallogr. Sect. C Struct. Chem.* **2019**, *75*, 777–782. [[CrossRef](#)]
44. Sanz, F.; Parada, C.; Rojo, J.M.; Ruiz-Valero, C. Crystal Structure, Magnetic Properties, and Ionic Conductivity of a New Mixed-Anion Phosphate $\text{Na}_4\text{Ni}_5(\text{PO}_4)_2(\text{P}_2\text{O}_7)_2$. *Chem. Mater.* **1999**, *11*, 2673–2679. [[CrossRef](#)]
45. Kanamori, J. Superexchange interaction and symmetry properties of electron orbitals. *J. Phys. Chem. Solids.* **1959**, *10*, 87–98. [[CrossRef](#)]
46. Anderson, P.W. New Approach to the Theory of Superexchange Interactions. *Phys. Rev.* **1959**, *115*, 2. [[CrossRef](#)]
47. Sanz, F.; Parada, C.; Rojo, J.M.; Ruíz-Valero, C. Synthesis, Structural Characterization, Magnetic Properties, and Ionic Conductivity of $\text{Na}_4\text{MII}_3(\text{PO}_4)_2(\text{P}_2\text{O}_7)$ (MII = Mn, Co, Ni). *Chem. Mater.* **2001**, *13*, 1334–1340. [[CrossRef](#)]
48. Goñi, A.; Lezama, L.; Barberis, G.E.; Pizarro, J.L.; Arriortua, M.I.; Rojo, T. Magnetic properties of the LiMPO_4 (M = Co, Ni) compounds. *J. Magn. Magn. Mater.* **1996**, *164*, 251–255. [[CrossRef](#)]

Disclaimer/Publisher’s Note: The statements, opinions and data contained in all publications are solely those of the individual author(s) and contributor(s) and not of MDPI and/or the editor(s). MDPI and/or the editor(s) disclaim responsibility for any injury to people or property resulting from any ideas, methods, instructions or products referred to in the content.